

# Quasi-three dimensional analysis of global instabilities: onset of vortex shedding behind a wavy cylinder

A. GARBARUK<sup>1</sup> AND J. D. CROUCH<sup>2†</sup>

<sup>1</sup>Saint-Petersburg State Polytechnic University, St Petersburg, 195220, Russia

<sup>2</sup>The Boeing Company, Seattle, WA 98124-2207, USA

(Received 21 January 2010; revised 19 January 2011; accepted 22 February 2011;  
first published online 19 April 2011)

In this paper the global-stability theory is extended to account for weak spanwise-flow variations using a quasi-three-dimensional framework. The analysis considers the onset of vortex shedding behind a circular cylinder with a spanwise-varying diameter. The quasi-three-dimensional approach models the fully three-dimensional flow structure as a series of two-dimensional eigenvalue problems representing the sectional-flow behaviour. The sectional results are coupled together using the Ginzburg–Landau equation, which models the diffusive coupling and provides the global response. The onset of global instability (and thus vortex shedding) is linked to both the sectional growth rates (characterized by the maximum-diameter location) and the spanwise extent of the zone of instability. Unsteady numerical simulations are used to guide the global-stability analysis and to assess the fidelity of the predictions. Results from the stability analysis are shown to be in good agreement with the numerical simulations, which are in close agreement with experiments.

**Key words:** flow–structure interactions, instability, vortex shedding

---

## 1. Introduction

The theory of global instabilities can be used to develop efficient and insightful methods for describing the early onset of complex unsteady-flow phenomena. In the works of Crouch, Garbaruk & Magidov (2007) and Crouch *et al.* (2009) an algorithm for the global-stability analysis of high-Reynolds-number turbulent flows on two-dimensional (2D) geometries is developed and successfully applied for prediction of transonic buffet onset. Although a generalization of this approach to arbitrary three-dimensional (3D) flows is in principal straightforward, its practical use is limited by the huge computational resources required for the full 3D eigenmode analysis. However, a wide class of flows of practical interest (e.g. flow past a swept wing) have a nearly homogeneous direction. This motivates an attempt at developing a simplified quasi-3D approach to global-stability analysis based on 2D cuts from a fully 3D steady flow field. This approximation is quite affordable in terms of computer resources and offers the potential for capturing the most important physics of the considered class of flows. However, the extension to quasi-3D flows introduces new questions regarding the boundary of unsteadiness and the degree of coupling in the nearly homogeneous direction.

This paper considers the onset of unsteadiness on a wavy cylinder as a simplified model problem to evaluate the quasi-3D analysis of global instabilities. A schematic

† Email address for correspondence: jeffrey.d.crouch@boeing.com



$D = D_0 + D_1 \cos(2\pi z/\lambda)$  (see figure 1). A measure of the spanwise variation is given by  $D_1/\lambda \ll 1$ . The cylinder is subjected to a uniform stream of velocity  $U$ . The maximum diameter  $D_{max} = D_0 + D_1$  and the velocity  $U$  are used to scale the results. This leads to the Reynolds number  $Re_{D_{max}} = UD_{max}/\nu$ , where  $\nu$  is the kinematic viscosity in the free stream.

Here we use the compressible-flow formulation to enable the application to more general flows of interest. All the results presented are based on a Mach number of  $M = 0.2$  and a Prandtl number of  $Pr = 0.71$ . The flow is governed by a set of five equations: continuity, streamwise momentum, transverse momentum, spanwise momentum and energy. These equations can be written in terms of the primitive variables, density  $\rho$ , streamwise velocity  $u$ , transverse velocity  $v$ , spanwise velocity  $w$  and temperature  $T$ , as follows:

$$\frac{\partial}{\partial t} M[\mathbf{q}] + Q[\mathbf{q}] + N[\mathbf{q}, \mathbf{q}] = 0, \quad (2.1)$$

where  $\mathbf{q} = \{\rho, u, v, w, T\}$ ,  $M$  and  $Q$  are the linear operators, and  $N$  contains all nonlinear terms.

The boundary conditions imposed on the surface of the body are

$$\left. \begin{aligned} u = v = w = 0, \\ \frac{\partial \rho}{\partial n} = \frac{\partial T}{\partial n} = 0, \end{aligned} \right\} \quad (2.2)$$

where  $\partial/\partial n$  is a derivative normal to the surface and the density condition is derived from the equation of state. The far-field conditions used in the compressible computations involve not only the primary variables  $\rho, u, v, w, T$  but also the Riemann invariants. Assuming spanwise-uniform flow at the outer boundaries, these conditions (expressed in terms of the primary variables) are given as

$$\left. \begin{aligned} I_1 = V_n + \frac{2a}{(\gamma - 1)} &= k_x u + k_y v + \frac{2}{(\gamma - 1)} \sqrt{\gamma RT}, \\ I_2 = V_n - \frac{2a}{(\gamma - 1)} &= k_x u + k_y v - \frac{2}{(\gamma - 1)} \sqrt{\gamma RT}, \\ I_3 = V_\tau = k_y u - k_x v, \quad I_4 = w, \quad I_5 = \frac{RT}{\rho^{\gamma-1}}. \end{aligned} \right\} \quad (2.3)$$

Here  $k_x, k_y$  are the local directional cosines of the boundary normal. These conditions are imposed on the subsonic boundaries in the following way. On the inlet boundary, the invariants  $I_1, I_3, I_4$  and  $I_5$  are given and  $I_2$  is extrapolated from the computational domain. On the outlet boundary,  $I_1, I_3, I_4$  and  $I_5$  are extrapolated from the computational domain and  $I_2$  is given.

The state vector describing the total flow field can be decomposed into a steady state  $\bar{\mathbf{q}} = \{\bar{\rho}, \bar{u}, \bar{v}, \bar{w}, \bar{T}\}$  and an unsteady vector  $\mathbf{q}' = \{\rho', u', v', w', T'\}$ ,  $\mathbf{q} = \bar{\mathbf{q}} + \mathbf{q}'$ . The vector  $\bar{\mathbf{q}}$  is a solution to the steady form of (2.1)–(2.3) – that is, with  $\partial \bar{\mathbf{q}}/\partial t \equiv 0$ . The steady-state Navier–Stokes equations are normally rewritten in conservative form before solving them numerically using the NTS code (Strelets 2001). This code is based on a finite-volume discretization on structured multi-block overlapping grids. The inviscid fluxes in the governing equations are approximated with the use of a third-order Roe scheme (Roe 1981), and the viscous fluxes are approximated with the second-order central difference scheme.

2.2. Quasi-3D approximation

The spanwise variation of the calculated baseflow  $\bar{q}$  is assumed to be small, as characterized by  $D_1/\lambda \ll 1$ . In the quasi-3D approximation, this small spanwise variation is treated as a parametric variation of  $\bar{q}$  with  $z$ , which neglects  $\partial\bar{q}/\partial z$  when calculating  $q'$ .

For conditions close to the steady state, the unsteady component  $q'$  can be considered a small perturbation to the vector  $\bar{q}$ . Substituting  $q = \bar{q} + q'$  into (2.1), cancelling the terms governing  $\bar{q}$ , neglecting the spanwise derivatives ( $\partial/\partial z$ ) on  $\bar{q}$  and linearizing the equations in terms of  $q'$  yields

$$\frac{\partial}{\partial t} M [q'] + N_{\bar{q}} [q'] = 0. \tag{2.4}$$

The linear operator  $M$  contains the terms associated with the time derivatives from the original equation (2.1). The linear operator  $N_{\bar{q}}$  consists of linear terms from the original equations and the terms generated by nonlinear interactions between  $\bar{q}$  and  $q'$ .

The quasi-3D approximation – neglecting the spanwise derivatives of the baseflow – leads to a flow field that is not a solution to the Navier–Stokes equations. Potential errors from this approximation will depend on the rate of spanwise variation as characterized, for example, by  $|\partial w/\partial z|$ . The level of  $|\partial w/\partial z|$ , in turn, will scale with the strength of the three-dimensionality,  $D_1/\lambda \ll 1$ . This is similar to the quasi-parallel approximation used in the boundary-layer stability theory (Crouch 1998). In that case, parallel-flow solutions that depend parametrically on the Reynolds number are used to approximate the growing (non-parallel) boundary layer. The fixed- $z$  cuts through the baseflow could be modified to solve the continuity equation, but this is not expected to impact the stability results for small values of  $D_1/\lambda$ .

The unsteady perturbation to the steady-state flow  $\bar{q}(x, y; z)$  at a section  $z$  can be represented by time-harmonic modes of the form

$$q'(x, y, t; z) = \hat{q}(x, y; z) \exp(-i\omega t). \tag{2.5}$$

The function  $\hat{q}$  describes the mode shape, and  $\omega$  is the frequency. In general, both  $\hat{q}$  and  $\omega$  can be complex, so the physical solution is taken as the real part of (2.5). Substituting (2.5) into (2.4) and rescaling the terms yields a system of equations for  $\hat{q}$  and  $\omega$ :

$$-i\omega\hat{q} + L(\bar{q})\hat{q} = 0, \tag{2.6}$$

with  $L$  being a second-order differential operator.

The boundary and far-field conditions are obtained by introducing  $q = \bar{q} + q'$  into expressions (2.2) and (2.3), cancelling the terms governing the steady state and linearizing with respect to  $q'$ . Then substituting (2.5) for  $q'$  yields the boundary conditions for  $\hat{q}$ :

$$\left. \begin{aligned} \hat{u} = \hat{v} = \hat{w} = 0, \\ \frac{\partial \hat{p}}{\partial n} = \frac{\partial \hat{T}}{\partial n} = 0. \end{aligned} \right\} \tag{2.7}$$

The far-field conditions for the inlet boundary are given by

$$\left. \begin{aligned} \hat{I}_1 = \hat{I}_3 = \hat{I}_4 = \hat{I}_5 = 0, \\ \frac{\partial \hat{I}_2}{\partial n} = 0, \end{aligned} \right\} \tag{2.8}$$

and for the outlet boundary by

$$\left. \begin{aligned} \frac{\partial \hat{I}_1}{\partial n} = \frac{\partial \hat{I}_3}{\partial n} = \frac{\partial \hat{I}_4}{\partial n} = \frac{\partial \hat{I}_5}{\partial n} = 0, \\ \hat{I}_2 = 0. \end{aligned} \right\} \quad (2.9)$$

The variables  $\hat{I}_1$ ,  $\hat{I}_2$ ,  $\hat{I}_3$ ,  $\hat{I}_4$  and  $\hat{I}_5$  are the linearized versions of the Riemann invariants, (2.3). Equations (2.6)–(2.9) describe an eigenvalue problem governing the complex frequency  $\omega$  and mode shape  $\hat{q}$  for a given  $z$ -section cut under the quasi-3D approximation.

### 2.3. Spanwise coupling and global response

The quasi-3D stability analysis yields a complex frequency  $\omega$  and an associated eigenfunction  $\hat{q}$  at each  $z$ -section. The 3D global instability depends on the entire zone of instability, and not just on a single cut through the cylinder. Thus, a solution for the physical problem requires some form of spanwise coupling to link the distinct cuts into a global response.

Earlier studies have shown that the diffusive spanwise coupling can be captured using model equations (Noack, Ohle & Eckelmann 1991; Albarède & Monkewitz 1992; Albarède & Provansal 1995). In the work of Albarède & Monkewitz (1992) the Ginzburg–Landau equation was used to capture the essential features of spanwise-limited shedding, including oblique shedding and the evolution of ‘chevron’ patterns in the cylinder wake.

Here, we exploit the linearized Ginzburg–Landau equation to construct the global response from the section-cut results. This equation can be written as

$$\frac{\partial}{\partial t} A = (\sigma_r + i\sigma_i) A + (\mu_r + i\mu_i) \frac{\partial^2}{\partial z^2} A, \quad (2.10)$$

with

$$\left. \begin{aligned} A(0, z) = A_0(z), \\ A(t, -L/2) = A(t, +L/2) = 0. \end{aligned} \right\} \quad (2.11)$$

The amplitude  $A$  represents any of the physical quantities in  $\hat{q}$ . Near the onset of instability, the sectional growth rate and frequency can be approximated by the values at the maximum-diameter location,  $\sigma = (\omega_i - i\omega_r)|_{z=0}$ . The complex constant  $\mu$  is a spanwise diffusion coefficient. The value of  $\mu$  (scaled with  $U$  and  $D_{max}$ ) can be linked to  $\bar{\mu}$  (scaled with  $D$  and  $\nu$ ), used in Albarède & Monkewitz (1992), by  $\mu = \bar{\mu}/Re_{Dmax}$ ; they show typical values of  $\bar{\mu}_r = 32 \pm 6$ , based on experiments with different end-plate boundary layers. The imaginary part of the diffusion coefficient is given by the ratio  $\bar{\mu}_i/\bar{\mu}_r = -0.3 \pm 0.6$ . The relatively large uncertainty is a carryover from the nonlinear term used in estimating the diffusion coefficient from fully nonlinear flow fields. Here, we will back out the value of  $\bar{\mu}_r$  by comparison to the simulations and use  $\bar{\mu}_i/\bar{\mu}_r = -1/3$ . The initial spanwise-amplitude distribution  $A_0(z)$  is given by uniform noise. The length  $L$  is taken to be the length over which the cylinder exhibits unstable section characteristics,  $l_{ins}$  (see §4.2), so the conditions at  $\pm L/2$  require the fluctuations to go to zero outside the ‘zone of instability.’

Following separation of variables, the solution of the Ginzburg–Landau equation is given by

$$\left. \begin{aligned} A(z, t) &= \sin\left(\frac{n\pi}{l_{ins}}\left(z + \frac{l_{ins}}{2}\right)\right) e^{\sigma_n t}, \\ \sigma_n &= \sigma - \mu\left(\frac{n\pi}{l_{ins}}\right)^2. \end{aligned} \right\} \quad (2.12)$$

Near the onset of instability, the  $n = 1$  term dominates the solution, and the global instability growth rate is given by

$$\sigma_{1r} = \sigma_r - \frac{\bar{\mu}_r}{Re_{D_{max}}}\left(\frac{\pi}{l_{ins}}\right)^2. \quad (2.13)$$

The value of  $\sigma_r$  is determined from the quasi-3D section-cut analysis at the maximum-diameter location. The value of  $l_{ins}$  describes the spanwise length of the zone of instability, in terms of diameters  $D_{max}$ . The value of  $\bar{\mu}_r = 12$  is obtained by comparison to one of the unsteady simulation cases; this gives  $\bar{\mu}_i = -4$ . The critical frequency is given by

$$\sigma_{1i} = \sigma_i - \frac{\bar{\mu}_i}{Re_{D_{max}}}\left(\frac{\pi}{l_{ins}}\right)^2. \quad (2.14)$$

For large wavelengths  $\lambda/D_{max}$  or small amplitude variations  $D_1/D_{max}$ , the instability length  $l_{ins}$  becomes large. In the limit of  $l_{ins}$  approaching infinity, the global growth rate approaches the sectional growth rate at the maximum-diameter location,  $\sigma_r = \omega_i$ , and the critical frequency approaches the section frequency at this location,  $\sigma_i = -\omega_r$ .

An alternative solution to (2.10) and (2.11) could be obtained by approximating  $\sigma$  with a cosine function in  $z$ . This leads to a Mathieu-type equation governing the spanwise variation. For the current focus on a single spanwise zone of instability – similar to the experiment of Chetan (2010) – this may not be justified. However, for the general periodic problem, this would allow for more complex spanwise variations – including subharmonics.

### 3. Unsteady simulations

The computations are carried out using the time-accurate version of the NTS code, described in §2.1 above. In this case, time integration is performed by an implicit second-order backward (three-layer) scheme with sub-iterations.

The size of the computational domain in the radial direction is equal to  $240D_0$ , and in the spanwise direction,  $z$ , it is equal to the half-period of the cosine wave,  $\lambda/2$  (symmetric boundary conditions are used at both  $z$ -boundaries). An example grid is shown in figure 2 (the grid has  $160 \times 200 \times 45$  nodes in the azimuthal, radial and spanwise directions respectively). The grid and size of the computational domain in the  $x$ – $y$  plane were shown to be sufficient for defining the critical value of the Reynolds number with an error less than 1% based on preliminary computations of the straight (2D) cylinder on different grids and with different domain sizes. The influence of the spanwise grid spacing was assessed by doubling the spanwise grid, which did not produce any visible alteration in the solution.

#### 3.1. Comparison to experiment

To assess the UNS solution, results of the computations are compared with the experimental data of Chetan (2010). Two cylinder models, long and short, were studied

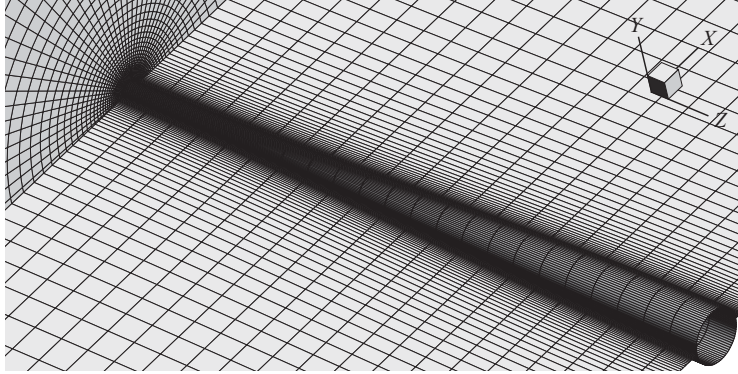


FIGURE 2. Typical cylinder grid, which covers a half-wavelength.

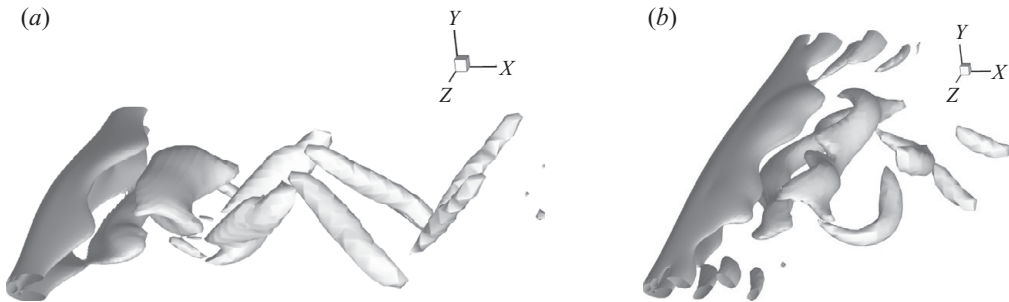


FIGURE 3. Isosurfaces of swirl from numerical simulations for the (a) short- and (b) long-wavelength cylinders at  $Re_{D_{max}} = 154$ .

in the experiments. The experimental models consisted of a single cosine wave, with constant-diameter end extensions. The cosine amplitude is given by  $D_1 = 0.33D_{max}$ , and the wavelengths are  $\lambda_{short} = 12.5D_{max}$  and  $\lambda_{long} = 25D_{max}$ .

Isosurfaces of the swirl quantity (magnitude of the second eigenvalue of the velocity gradient tensor) are presented in figure 3 for both the short and long cylinders at  $Re_{D_{max}} = 154$ . Both cases are well above the critical conditions for the onset of shedding. The images show that the shedding fluctuations are more dominant in the middle of the cylinder, around the maximum-diameter location. The near-field wake shows a spanwise wavy structure, which evolves into a more complex 3D flow field downstream. For larger values of  $\lambda/D_{max}$ , the shedding fluctuations are more concentrated around the maximum-diameter location. The harmonic nature of the shedding is shown in the time-series plots of figure 4. For the short-wavelength cylinder, the shedding is characterized by a single frequency – roughly scaling with the maximum diameter. This is consistent with the observations in the experiments of Chetan (2010). For the long-wavelength cylinder, there are two characteristic frequencies: one associated with the maximum diameter and one with the minimum diameter. Note that at this Reynolds number, a 2D cut through the cylinder would suggest that the minimum-diameter section is also supercritical.

Figure 5 provides a detailed comparison of the numerical predictions with the experimental data. The figure shows the computed and measured contours of the instantaneous velocity magnitude for the short cylinder at two values of the Reynolds number based on the maximum diameter of the cylinder – one close to the onset

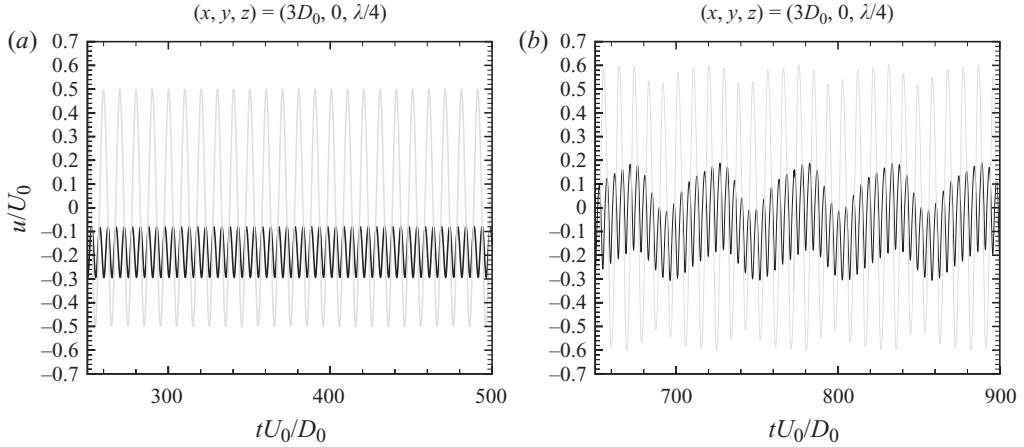


FIGURE 4. Time histories of velocity components from simulations of short- (a) and long-wavelength (b) cylinders at  $Re_{D_{max}} = 154$ .

of unsteadiness and the other corresponding to the strongly unsteady (supercritical) regime. One can see that in both cases, predicted and measured flow patterns are not only qualitatively similar but also quantitatively close.

Thus, in general, the comparison with experiments provides good support for the current numerical approach, which is used for both the baseflow calculation and the UNS for assessing the stability theory.

### 3.2. Onset of vortex shedding

The critical Reynolds number for the onset of shedding is estimated from the UNS solutions to be  $Re_{D_{max}} \approx 55.5\text{--}57$  for the long-wavelength cylinder and  $Re_{D_{max}} \approx 69\text{--}70.5$  for the short-wavelength cylinder. By comparison, the critical Reynolds number for a 2D cylinder is  $Re_D = 47$  (Hammache & Gharib 1991; Crouch *et al.* 2007). The experiments show critical Reynolds numbers of approximately 59 and 61 for the long- and short-wavelength cylinders, respectively. For the long-wavelength cylinder, the agreement is reasonably good, but for the short-wavelength one, the computed critical Reynolds number is significantly overestimated. This may be explained by the difference between the numerical and experimental set-ups. In the simulations, the cylinders have purely cosine profiles and are periodic in the spanwise direction, whereas the experimental models have constant-diameter tips with length  $2.5D_{max}$  (0.015 m). The tip effects are expected to be more significant for the shorter wavelength cylinder.

Analysis of the UNS results show that in both initial (linear) and developed stages, the flow oscillations are harmonic with frequency  $\omega_r = 0.69$  (scaled with  $D_{max}$ ) which is very close to the value  $\omega_r = 0.73$  obtained earlier for the straight cylinder (Crouch *et al.* 2007). This is seen in figure 6, which shows snapshots of the azimuthal velocity component in the symmetry plane of the cylinder in the initial and developed stages. One can see that the velocity field in both stages is qualitatively the same (the only difference between the two snapshots is the much higher amplitude of the oscillations in the developed stage). This suggests that near the onset of shedding, the global oscillations of the flow past the wavy cylinder are governed by its most unstable (maximum-diameter) section.

The wave fronts of the velocity oscillations in figure 6 are curved, roughly following a cosine variation. The variation of the constant-phase lines over a half-wavelength

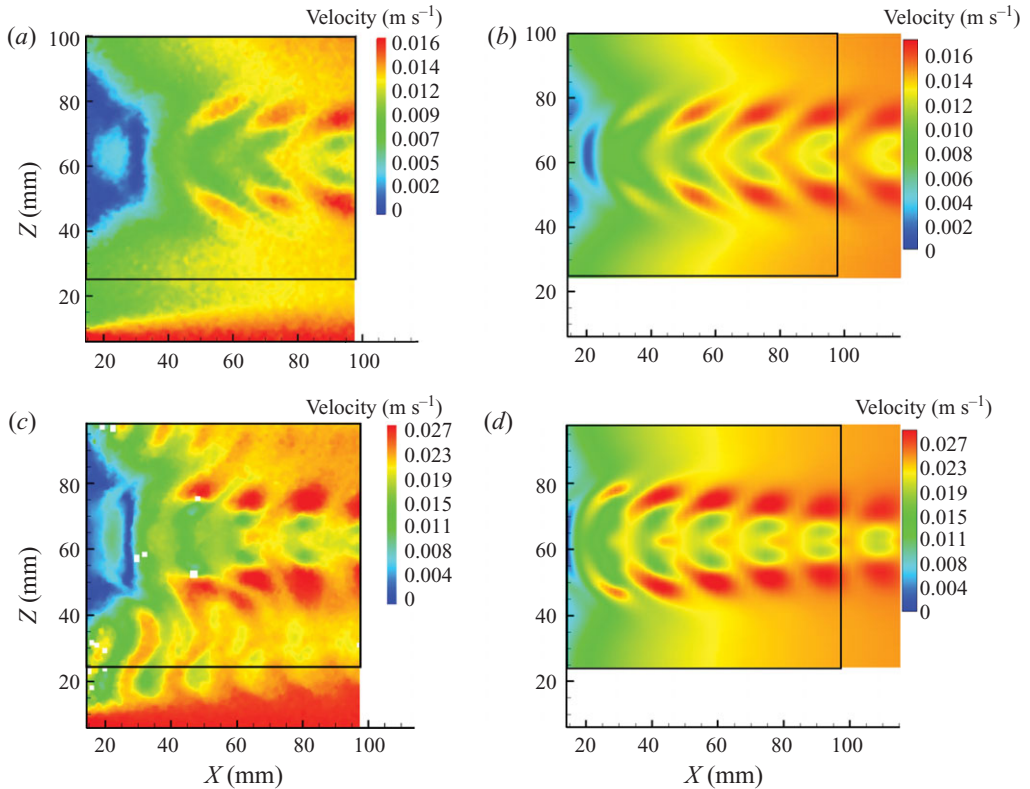


FIGURE 5. Snapshots of the velocity magnitude for the short-wavelength cylinder at (a,b)  $Re_{D_{max}} = 90$  and (c,d)  $Re_{D_{max}} = 154$ . (a,c) Images from the experiment of Chetan (2010), and (b,d) images from the simulations. The rectangular ‘window’ shows the region where comparison can be made, and  $z = 62.5$  mm corresponds to  $D_{max}$ .

(from maximum diameter to minimum diameter) is in qualitative agreement with experimental observations for the flow over a cone (Papangelou 1992).

Figure 7 shows a plot of the spanwise variation of normalized amplitude for the azimuthal velocity oscillations, taken in the symmetry plane at a distance  $1.4D_{max}$  downstream of the cylinder. The figure shows that in the close downstream vicinity of the cylinder the amplitude is virtually zero at the minimum-diameter locations, where the local Reynolds number is near critical (based on a 2D straight-cylinder approximation). Farther downstream, the region of non-zero oscillations slowly widens. The spanwise extent of the unsteadiness can be characterized by a length scale  $l_{uns} = \int_{-\lambda/2}^{\lambda/2} A(z)/A_{max} dz$ . The calculated  $l_{uns}$  for figure 7 gives  $l_{uns}/\lambda = 0.27$  for  $\lambda/D_{max} = 60$  and  $l_{uns}/\lambda = 0.42$  for  $\lambda/D_{max} = 15$ .

The above observations suggest that, at least for the considered geometry, the unsteadiness of the wavy-cylinder flow is mostly associated with the maximum-diameter section, which provides support for the viability of a sectional analysis for the stability. On the other hand, it is clear that such an analysis, either 2D or quasi-3D, carried out for only one section of the flow is insufficient. For instance, even if the maximum Reynolds number  $Re_{D_{max}}$  for a wavy-cylinder flow is larger than the critical value of 47 for the straight cylinder, the flow may still remain stable. In other words, in addition to  $Re_{D_{max}}$ , the onset of unsteadiness of the flow past a

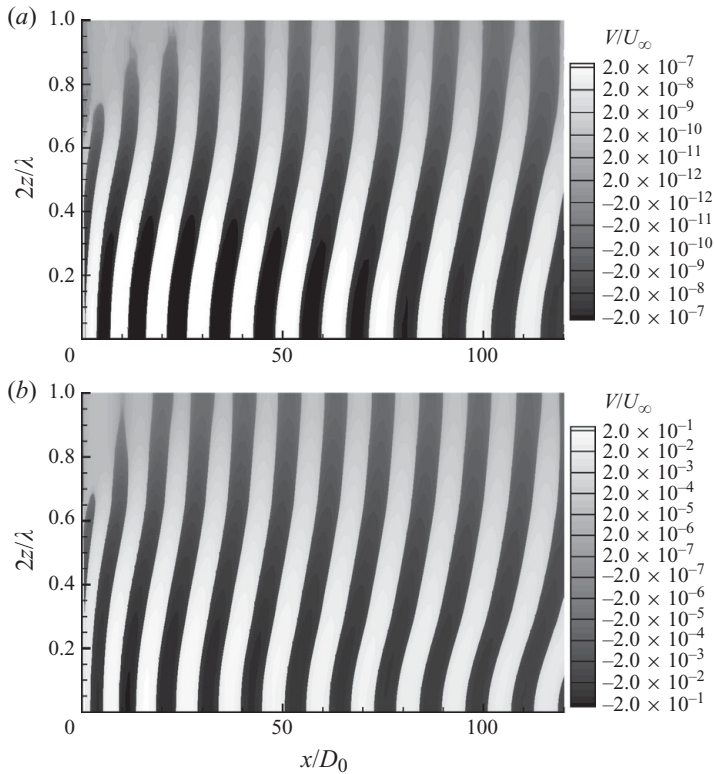


FIGURE 6. Instantaneous contours of azimuthal velocity in the symmetry plane of the cylinder, taken from numerical simulations in the linear (a) and fully developed (b) stages of shedding development. Results for the long cylinder with  $D_{max}$  at  $z=0$  and  $Re_{D_{max}} = 60$ .

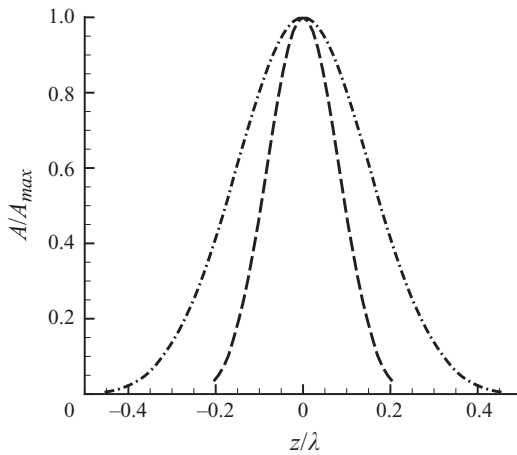


FIGURE 7. Spanwise variation of the normalized velocity-fluctuation amplitude for the azimuthal component measured  $1.4D_{max}$  downstream of the cylinder, from numerical simulations. Results for  $D_1/D_{max} = 0.2$ , with  $\lambda/D_{max} = 60$ ,  $Re_{D_{max}} = 51.25$  (dashed curve), and  $\lambda/D_{max} = 15$ ,  $Re_{D_{max}} = 58.75$  (dash-dotted curve).

---

$D_1/D_{max}$	$\lambda/D_{max}$	$D_1/\lambda$	$Re_{D_{max}}^{crit}$
0.20	60	0.0033	50.0–51.25
0.20	30	0.0067	52.5–53.75
0.20	15	0.0133	57.5–58.75
0.33	50	0.0067	51.0–52.50
0.33	25	0.0133	55.5–57.00
0.33	12.5	0.0267	72.0–73.50

---

TABLE 1. Summary of the conditions investigated using the UNS code.

wavy cylinder depends on its geometry, namely on  $D_1/D_{max}$  and  $\lambda/D_{max}$ . In order to elucidate the effect of these parameters and to obtain benchmark data for assessing the stability theory, a series of UNS computations are conducted. These include two sets of computations at  $D_1/D_{max}$  equal to 0.2 and 0.33 performed at different values of  $\lambda/D_{max}$  (from 12.5 to 60). Each case has been computed at different values of  $Re_{D_{max}}$ , which permits an identification of the critical  $Re_{D_{max}}$  value (corresponding to the onset of unsteadiness). Table 1 provides a summary of the unsteady-simulation results.

As expected, for all the cases considered, the UNS predictions of the critical Reynolds number,  $Re_{D_{max}}^{crit}$ , are higher than the critical value of 47 for the straight cylinder. In other words, the wavy-cylinder flow is always more stable than the corresponding 2D cylinder flow (with diameter equal to  $D_{max}$ ). At fixed  $D_1/D_{max}$ , an increase of  $\lambda/D_{max}$  results in a decrease of  $Re_{D_{max}}^{crit}$ . This is expected since an increase in  $\lambda/D_{max}$  at fixed  $D_1/D_{max}$  results in less pronounced three-dimensionality of the flow, so the critical value  $Re_{D_{max}}^{crit}$  should approach the critical value for a straight cylinder. Finally, independent of the  $\lambda/D_{max}$  value, an increase of the parameter  $D_1/D_{max}$  leads to an increase of the critical Reynolds number. Both these trends can be attributed to the increase of the flow three-dimensionality with the growth of the parameter  $D_1/\lambda$ , which characterizes the rate of spanwise variation of the geometry. For larger values of  $D_1/\lambda$ , the critical Reynolds number scales more closely with  $D_0$  than  $D_{max}$ .

## 4. Quasi-3D stability analysis

### 4.1. Steady baseflow solutions

In order to conduct a global-stability analysis, steady baseflow solutions are required. An example of a 3D steady solution obtained for the long cylinder considered above ( $D_1/D_{max} = 0.33$ ,  $\lambda/D_{max} = 25$ ) at  $Re_{D_{max}} = 60$  is presented in figure 8. The figure compares the contours of the streamwise velocity component at three spanwise sections corresponding to the minimum, mid and maximum cylinder diameter. Similar contours from computations of three 2D (straight) cylinders with the same diameters are also shown. The cuts of the 3D flow field and the corresponding 2D solutions, while visually similar, turn out to be significantly different (in terms of the stability characteristics). However, the peak value in the spanwise velocity (not shown) is only about 8% of the free-stream velocity. As a measure for the level of three-dimensionality, the maximum value of  $|\partial w/\partial z|$  at the maximum-diameter location is 0.016 relative to  $|\partial u/\partial x|$  and  $|\partial v/\partial y|$  of order 1. As expected, the magnitude of the spanwise-velocity derivative scales with  $D_1/\lambda$ .

For this case, the Reynolds number based on the local diameter varies along the cylinder from 60 down to 20, i.e. in a rather wide range around the critical value of

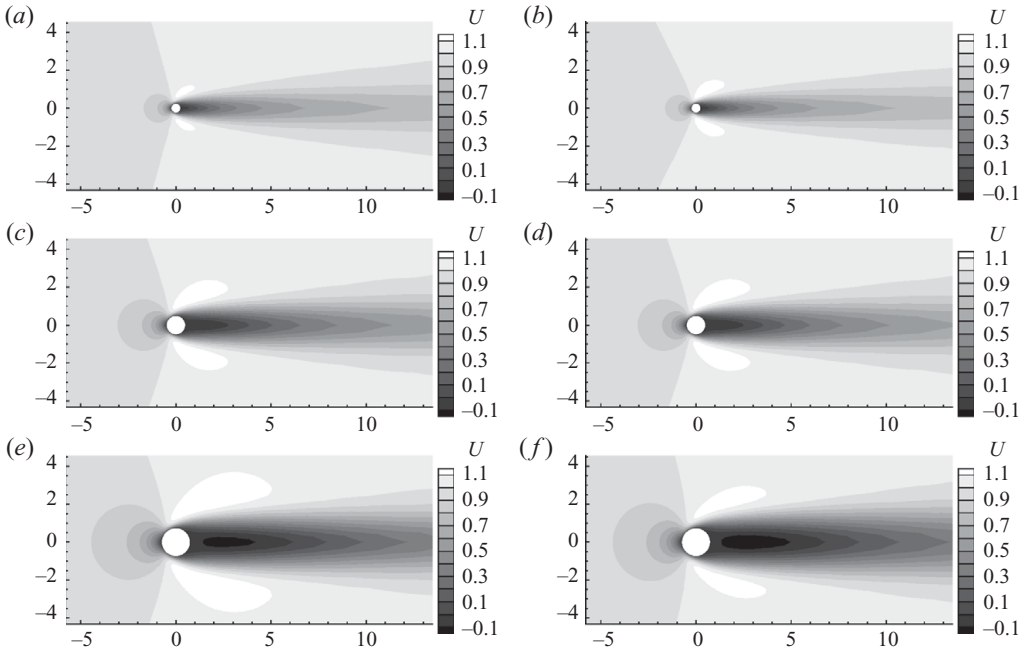


FIGURE 8. Comparison of the calculated streamwise velocity of the baseflow for a wavy cylinder (*a,c,e*) at (*a,b*)  $z = -\lambda/2$ , (*c,d*)  $z = -\lambda/4$  and (*e,f*)  $z = 0$ . 2D calculations for straight cylinders with matching diameters are also shown (*b,d,f*).

about 47 for the straight cylinder. Along with the steady solution, a time-accurate simulation of the same flow was carried out starting from the converged (with the residual less than  $10^{-10}$ ) steady-state solution. As expected, an unsteady solution is obtained, thus suggesting that at the considered value of  $Re_{D_{max}} = 60$  the flow over the wavy cylinder is globally unstable.

#### 4.2. Stability results

The stability calculations start with a steady 3D flow field similar to that in figure 8. Fixed- $z$  station cuts are extracted from this flow field for use in the quasi-3D stability analysis. For each cut, (2.6)–(2.9) are solved for the sectional-stability characteristics subject to a spanwise-uniform-flow approximation (i.e.  $\partial/\partial z$  is neglected). The combined section-cut results are then used to determine the global-stability characteristics using (2.13) and (2.14).

Results from the section-stability analysis of the 3D wavy-cylinder flow field are given in figure 9 for  $\lambda/D_{max} = 60$ ,  $Re_{D_{max}} = 50$ . At these conditions, the UNS show the flow to be steady, implying global stability. The figure shows the growth rate as a function of  $z$ , along with the corresponding section of the cylinder. The solid curve gives the quasi-3D result, and the short-dashed curve is for a 2D (straight) cylinder with a diameter matching the local-section diameter. The long-dashed line shows the growth rate for a straight cylinder with a diameter matching  $D_{max}$ . The taper ( $D < D_{max}$  for  $|z| > 0$ ) has a stabilizing effect in terms of the sectional growth rate. This stabilizing effect will increase in relation to the level of taper – characterized by  $D_1/\lambda$ . Thus, the wavy cylinder displays a ‘zone of instability’, which can be characterized by the spanwise length  $l_{ins}$ , over which  $\omega_i > 0$ . At the maximum-diameter location, the growth rate predicted from the quasi-3D analysis is greater than the 2D result

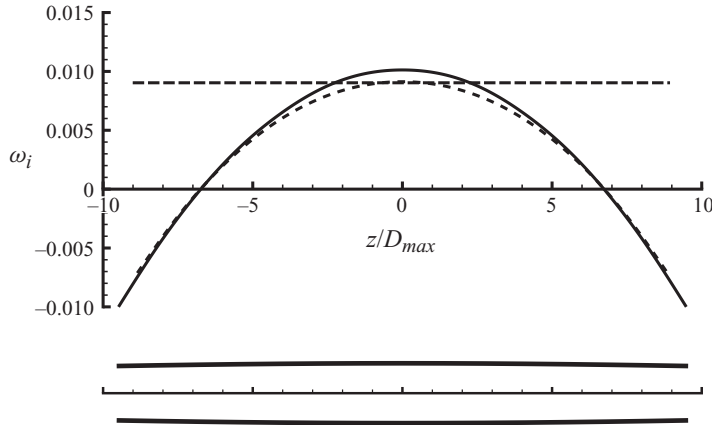


FIGURE 9. Sectional growth rates based on the quasi-3D analysis (solid line), approximate-2D analysis (short-dashed line) and 2D analysis for  $D = D_{max}$  (long-dashed line). Variation of the cylinder diameter is also shown for reference ( $D_1/D_{max} = 0.2$ ,  $\lambda/D_{max} = 60$ ,  $Re_{D_{max}} = 50$ ).

for  $D = D_{max}$ . The  $x$ - $y$  structure of the unsteadiness is given by the eigenfunction  $\hat{q}$ . This structure is consistent with the typical vortex shedding pattern, as discussed in Crouch *et al.* (2007).

Figure 10 shows stability results for a range of  $\lambda/D_{max}$  and  $D_1/D_{max}$  values. In each case, the Reynolds number is close to the value where the flow first becomes unsteady in the UNS. At these near-critical conditions, the values of  $\omega_i$  at  $D = D_{max}$  and  $l_{ins}$  vary significantly with the degree of three-dimensionality. The results from figure 10 also show that the differences between the quasi-3D analysis and the approximate-2D analysis increase significantly with the level of three-dimensionality (for near-critical conditions). In figure 10(a) (with  $D_1/\lambda = 0.0033$ ), the quasi-3D result is indistinguishable from the approximate-2D result. In figure 10(f) (with  $D_1/\lambda = 0.026$ ), the maximum values of  $\omega_i$  differ by nearly a factor of 2.

Figure 10 also shows the frequencies  $\omega_r$  calculated from the sectional analysis. For comparison, the frequency observed in the UNS is shown by a straight line extending over the length of the zone of unsteadiness  $l_{uns}$ . The quasi-3D results for the frequency at the  $D = D_{max}$  section are in general agreement with the UNS results.

The length of unsteadiness  $l_{uns}$  (from the UNS) is compared to the length of instability  $l_{ins}$  (from the section-stability analysis) in figure 11. The values are plotted as a function of the level of three-dimensionality  $D_1/\lambda$ ; the lines are power-curve fits through the points. The two curves follow one another very closely, suggesting a link between the global unsteadiness and the zone of instability predicted by the section-cut analysis.

### 4.3. Spanwise coupling and global response

In the quasi-3D analysis, the global response is obtained from the section-cut stability results by accounting for the spanwise coupling of the flow. This is modelled using the Ginzburg–Landau equation, which yields a spanwise-amplitude function, a growth rate and a frequency for the unsteady flow quantity. The amplitude function, given in (2.12), is plotted in figure 12 for the two flow conditions considered in figure 7. Here the spanwise variable is normalized with the maximum diameter, as compared to the waviness wavelength used in figure 7. The agreement around the maximum-diameter location is very good. The key difference between the theory and simulation occurs at

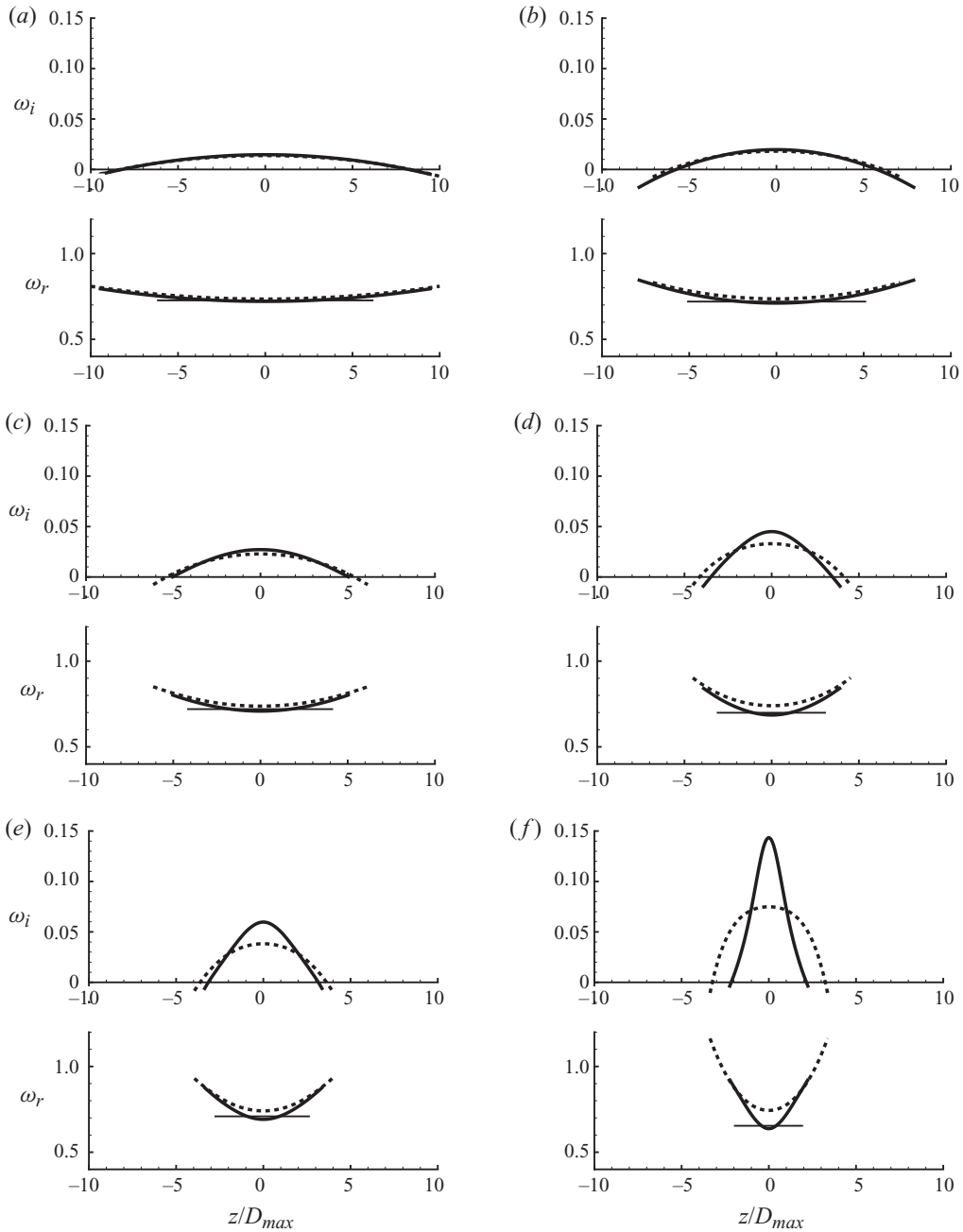


FIGURE 10. Sectional growth rates and frequencies at near-critical conditions (just supercritical as determined from the UNS) for: (a)  $D_1/D_{max} = 0.20$ ,  $\lambda/D_{max} = 60$ ,  $Re_{D_{max}} = 51.25$ ; (b)  $D_1/D_{max} = 0.33$ ,  $\lambda/D_{max} = 50$ ,  $Re_{D_{max}} = 52.5$ ; (c)  $D_1/D_{max} = 0.20$ ,  $\lambda/D_{max} = 30$ ,  $Re_{D_{max}} = 53.75$ ; (d)  $D_1/D_{max} = 0.33$ ,  $\lambda/D_{max} = 25$ ,  $Re_{D_{max}} = 57$ ; (e)  $D_1/D_{max} = 0.20$ ,  $\lambda/D_{max} = 15$ ,  $Re_{D_{max}} = 58.75$ ; and (f)  $D_1/D_{max} = 0.33$ ,  $\lambda/D_{max} = 12.5$ ,  $Re_{D_{max}} = 73.5$ . The thick-solid-line results are from the quasi-3D analysis, the dashed-line results are from the approximate-2D analysis and the thin solid line shows the frequency and the zone of unsteadiness from the simulations.

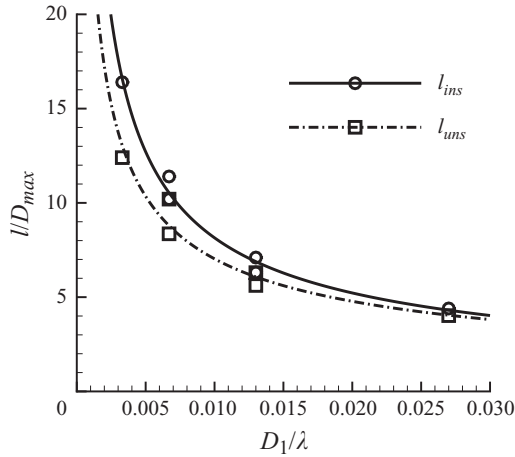


FIGURE 11. Variation of the length of unsteadiness ( $l_{ums}$  from simulations) and the length of instability ( $l_{ins}$  from the quasi-3D analysis) as a function of the level of three-dimensionality  $D_1/\lambda$ .

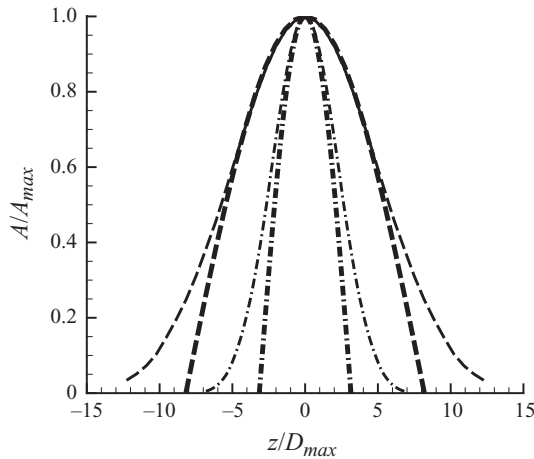


FIGURE 12. Spanwise variation of the normalized velocity-fluctuation amplitude as predicted from the stability theory (thick lines) and from the UNS (thin lines). Results for  $D_1/D_{max} = 0.2$ , with  $\lambda/D_{max} = 60$ ,  $Re_{D_{max}} = 51.25$  (dashed curves) and  $\lambda/D_{max} = 15$ ,  $Re_{D_{max}} = 58.75$  (dash-dotted curves).

the edges of the unsteadiness; the theory predicts a sharp cutoff, while the simulations show a low-amplitude ‘tail’ in the spanwise response.

Figure 13 shows the critical Reynolds number as a function of  $\lambda/D_{max}$  calculated from (2.13) using the results of figure 10. The two curves show two different values of  $D_1/D_{max}$ . The symbols are from the UNS solutions. The open symbols correspond to the conditions that are found to be unsteady, and the filled symbols are for the conditions that resulted in steady solutions. The straight dashed line shows the large-wavelength limiting value (from 2D analysis). In general, the agreement with the simulations is very good. As the flow becomes more 3D (smaller  $\lambda/D_{max}$  or larger  $D_1/D_{max}$ ), the differences between the theory and simulation become more significant.

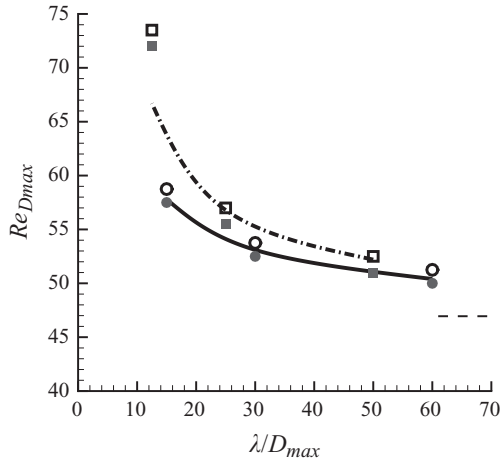


FIGURE 13. Critical Reynolds number for the onset of vortex shedding as predicted by the stability theory (lines) and the UNS (solid symbols – steady, open symbols – unsteady). The solid line and circles correspond to  $D_1/D_{max} = 0.20$ , and the dashed line and squares correspond to  $D_1/D_{max} = 0.33$ .

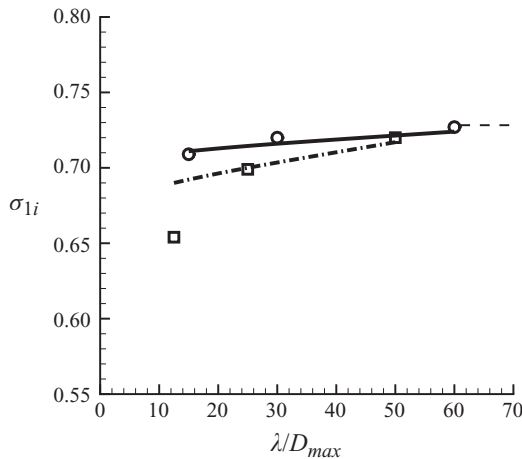


FIGURE 14. Critical frequency for global mode at the onset of vortex shedding as predicted by the stability theory (lines) and the UNS (symbols). The solid line and circles correspond to  $D_1/D_{max} = 0.20$ , and the dashed line and squares correspond to  $D_1/D_{max} = 0.33$ .

The critical frequencies corresponding to figure 13 are shown in figure 14. These also show good agreement between the theory and simulations.

### 5. Conclusions

In this paper, the global-stability analysis is extended from 2D baseflows to 3D baseflows, with a weak variation in a third (spanwise) dimension, using a quasi-3D formulation. The spanwise variation is modelled parametrically, leading to 2D stability problems that are solved at discrete spanwise sections. The global response is constructed using the Ginzburg–Landau equation to model the spanwise diffusive coupling between the sections.

This approach is used to analyse the onset of vortex shedding for a circular cylinder with the diameter varying periodically along the cylinder axis. The global-instability growth rate, and the associated frequency, for a wavy cylinder is a function of the sectional growth rate at the maximum-diameter location and the spanwise extent of the instability. Stability-based predictions for the onset of vortex shedding on the wavy cylinder are in very good agreement with direct numerical simulations. The stability analysis and the numerical simulations both show a spanwise-limited zone of unsteadiness at the onset of shedding. This zone becomes smaller with an increasing level of three-dimensionality, characterized by the waviness amplitude or the inverse of the wavelength. The critical Reynolds number for vortex shedding increases with the level of three-dimensionality, while the critical frequency drops.

We would like to acknowledge helpful discussions with Professor Mike Gaster, Professor O.N. Ramesh and Professor Peter Monkewitz.

#### REFERENCES

- ALBARÈDE, P. & MONKEWITZ, P. A. 1992 A model for the formation of oblique shedding and chevron patterns in cylinder wakes. *Phys. Fluids A* **4**, 744–756.
- ALBARÈDE, P. & PROVANSAL, M. 1995 Quasi-periodic cylinder wakes and the Ginzburg–Landau model. *J. Fluid Mech.* **291**, 191–222.
- CHETAN, S. J. 2010 Dynamics of vortex shedding from slender cones. Ph.D. Dissertation, University of London.
- CROUCH, J. D. 1998 Theory of instability and transition. In *The Handbook of Fluid Dynamics* (ed. R. W. Johnson), pp. 13-12–13-25, CRC Press.
- CROUCH, J. D., GARBARUK, A. & MAGIDOV, D. 2007 Predicting the onset of flow unsteadiness based on global instability. *J. Comput. Phys.* **224**, 924–940.
- CROUCH, J. D., GARBARUK, A., MAGIDOV, D. & TRAVIN, A. 2009 Origin of transonic buffet on aerofoils. *J. Fluid Mech.* **628**, 357–369.
- GASTER, M. 1969 Vortex shedding from slender cones at low Reynolds numbers. *J. Fluid Mech.* **38**, 565–576.
- HAMMACHE, M. & GHARIB, M. 1991 An experimental study of the parallel and oblique vortex shedding from circular cylinders. *J. Fluid Mech.* **232**, 567–590.
- JACKSON, C. P. 1987 A finite-element study of the onset of vortex shedding in flow past variously shaped bodies. *J. Fluid Mech.* **182**, 23–45.
- NOACK, B. R., OHLE, F. & ECKELMANN, H. 1991 On cell formation in vortex streets. *J. Fluid Mech.* **227**, 293–308.
- PAPANGELOU, A. 1992 Vortex shedding from slender cones at low Reynolds numbers. *J. Fluid Mech.* **242**, 299–321.
- ROE, P. L. 1981 Approximate Riemann solvers, parameters vectors and difference schemes. *J. Comput. Phys.* **43**, 357–372.
- STRELETS, M. 2001 Detached-eddy simulation of massively separated flows. *AIAA Paper* 2001-0879.
- WILLIAMSON, C. H. K. 1989 Oblique and parallel modes of vortex shedding in the wake of a circular cylinder at low Reynolds numbers. *J. Fluid Mech.* **206**, 579.
- ZEBIB, A. 1987 Stability of viscous flow past a circular cylinder. *J. Engng Math.* **21**, 155–165.